

Statistical characterization and classification of astronomical transients with Machine Learning in the era of the Vera C. Rubin Observatory

Marco Vicedomini, Massimo Brescia, Stefano Cavuoti, Giuseppe Riccio, Giuseppe Longo

Preprint version of the manuscript to appear in the Volume “Intelligent Astrophysics” of the series “Emergence, Complexity and Computation”, Book eds. I. Zelinka, D. Baron, M. Brescia, Springer Nature Switzerland, ISSN: 2194-7287

Abstract Astronomy has entered the multi-messenger data era and Machine Learning has found widespread use in a large variety of applications. The exploitation of synoptic (multi-band and multi-epoch) surveys, like LSST (Legacy Survey of Space and Time), requires an extensive use of automatic methods for data processing and interpretation. With data volumes in the petabyte domain, the discrimination of time-critical information has already exceeded the capabilities of human operators and crowds of scientists have extreme difficulty to manage such amounts of data in multi-dimensional domains. This work is focused on an analysis of critical aspects related to the approach, based on Machine Learning, to variable sky sources classification, with special care to the various types of Supernovae, one of the most important subjects of Time Domain Astronomy, due to their crucial role in Cosmology. The work is based on a test campaign performed on simulated data. The classification was carried out by comparing the performances among several Machine Learning algorithms on statistical parameters extracted from the light curves. The results make in evidence some critical aspects related to the data quality and their parameter space characterization, propaedeutic to the preparation of processing machinery for the real data exploitation in the incoming decade.

M. Vicedomini, S. Cavuoti and G. Longo
Department of Physics, University of Naples Federico II, Strada Vicinale Cupa Cintia, 21, I-80126 Napoli, Italy. e-mail: stefano.cavuoti@inaf.it

M. Brescia and G. Riccio
INAF - Astronomical Observatory of Capodimonte, Salita Moiariello 16, I-80131 Napoli, Italy. e-mail: massimo.brescia@inaf.it

1 Introduction

The scientific topics covered in this work falls within what is called Time Domain Astronomy. This is the study of variable sources, i.e. astronomical objects whose light changes with time. Although the taxonomy of such sources is extremely rich, there are two main kinds of objects, respectively, transients and variables. The first changes its nature during the event, while the second presents just a brightness variation. The study of these phenomena is fundamental to identify and analyze either the mechanisms causing light variations and the progenitors of the various classes of objects.

Since ancient times the phenomenon of Supernovae (SNe) has fascinated human beings, but only recently we understood, in most cases, why and how this explosion happens [1]. Obviously there are still many open questions, but the knowledge about the type of galaxy hosting various kinds of Supernova and at which rate they take place, could help us to better understand this phenomenon and many other related properties of the Universe [2].

For example, the observed luminosity dispersion of SNe is evidenced through inhomogeneities in the weak lensing event and this is an upper limit on the cosmic matter power spectrum. Massive cosmological objects like galaxies and clusters of galaxies can magnify many times the flux of events like SNe that would be too faint to detect and bring them into our analysis scope. Studies on lensed SNe type Ia by clusters of galaxies may be used to probe the distribution of dark matter on them. Time delay between the multiple images of lensed SNe could provide a good estimates of its high redshift. Furthermore there are two factors that makes SNe better than other sources, like quasars, in measuring time delay [3]: *(i)* if the Supernovae is taken before the peak, the measurements are easier and on short timescale compared to the quasars; *(ii)* the SN light fade away with time, so we can measure the lens stellar kinematics and the dynamics lens mass modeling. In the next decade, the Vera C. Rubin Observatory will perform the Rubin Observatory Legacy Survey of Space and Time (LSST), using the Rubin Observatory LSST Camera and the Simonyi Survey Telescope. LSST will play a key role in the discovery of new lensed SNe Ia [4]. LSST will help to find apparently host-less SNe of every type, and this may help to study dwarf galaxies with a mass range of $10^4 \div 10^6$ solar masses. These galaxies, indeed, play a key role in large scale structure models, and despite their very big predicted population, over 1 Mpc we cannot see them until now. Same story for the theorized intracluster population of stars stripped from their galaxies, which could be seen through the SNe host-less events.

In order to understand and push ourselves further and further into the universe, ever more powerful incoming observing instruments, like LSST, will be able to deliver impressive amounts of data, for which astronomers are obliged to make an intensive use of automatic analysis systems. Methods that fall under the heading Data Mining and Machine Learning have now become commonplace and indispensable to the work of scientists [5, 6, 7]. But then, where the human work is still needed? For sure in terms of final analysis and validation of the results. This thesis work is therefore based on this virtuous combination, by exploiting data science methodology

and models, such as Random Forest [8], Nadam, RMSProp and Adadelta [9], to perform a deep investigation on time domain astronomy, by focusing the attention on Supernovae classification, performed on realistic sky simulations. Furthermore, a special care has been devoted to the parameter space analysis, through the application of the method Φ LAB [10, 11] to the various classification experiments, in order to evaluate the commonalities among them in terms of features found as relevant to solve the recognition of different types of transients.

In Sec. 2 we describe the two data simulations used for the experiments and the extracted statistical features composing the data parameter space. In Sec. 3 we give a brief introduction of the ML methods used, while in Sec. 4 the series of experiments performed are deeply reported. Finally, in Sec. 5 we analyze the results and draw the conclusions.

2 Data

In this work two simulation datasets were used; the Supernova Photometric Classification Challenge (hereafter SNPhotCC, [12]) and the Photometric LSST Astronomical Time-Series Classification Challenge (hereafter PLAsTiCC, [13, 14, 15]).

2.1 The SNPhotCC simulated catalogue

This catalogue was the subject of a challenge performed in 2010 and consists of a mixed set of simulated SN types, respectively, Ia, Ibc and II, selected by respecting the relative rate (Table 1). The volumetric rate was found by Dilday et al. [16] as $r_v = \alpha(1+z)^\beta$, where for SNe Ia parameters we have $\alpha_{Ia} = 2.6 \times 10^{-5} Mpc^{-3} h_{70}^3 yr^{-1}$, $\beta_{Ia} = 1.5$ and $h_{70} = H_0 / (70 km s^{-1} Mpc^{-1})$. H_0 is the present value of the Hubble parameter. For non Ia SNe, the parameters come from Bazin et al. [17] and are $\alpha_{NonIa} = 6.8 \times 10^{-5} Mpc^{-3} h_{70}^3 yr^{-1}$ and $\beta_{NonIa} = 3.6$. The simulation is based on four bands, *griz*, with cosmological parameters $\Omega_M = 0.3$, $\Omega_\Lambda = 0.7$ and $\omega = -1$, where Ω_M is the density of barionic and dark matter, Ω_Λ is the density of dark energy and ω is the cosmological constant. Moreover, the point-spread function, atmospheric transparency and sky-noise were measured in each filter and epoch using the one-year chronology.

Types	Bands	Sampling	%	Amount
SNIa	g,r,i,z	uneven	23,86	5088
SNIbc	g,r,i,z	uneven	13,14	2801
SNII	g,r,i,z	uneven	63	13430

Table 1 SNPhotCC dataset composition.

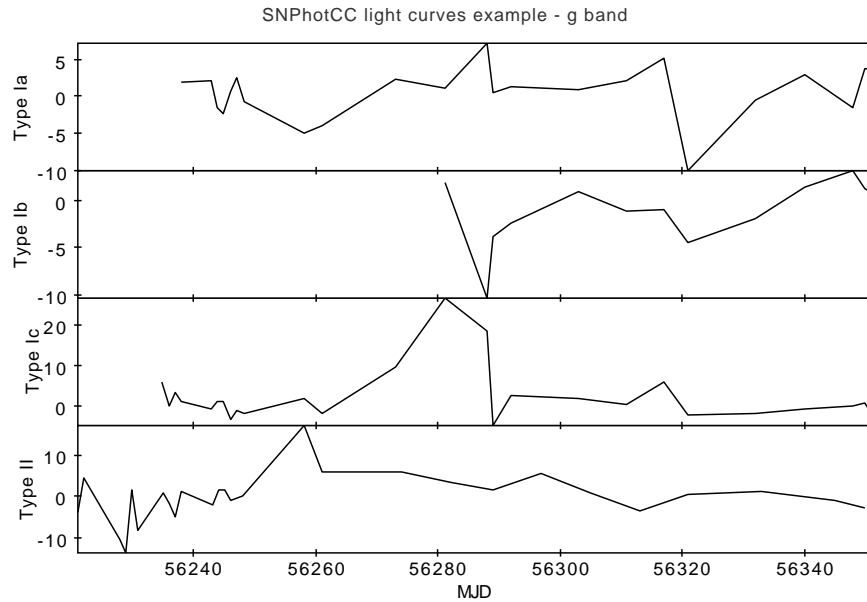


Fig. 1 Examples of SNPhotCC light curves in *g* band. From the top to the bottom: SN004923(Ia), SN000760(Ib), SN003475(Ic), SN001986(II).

The dataset sources are based on two variants, respectively, with or without the host-galaxy photometric redshift. For this work only the samples without redshift information were used.

Every simulated light curve has at least one observation, in two or more bands, with signal-to-noise ratio > 5 and five observations after the explosion (Fig. 1). A spectroscopically confirmed training subset was provided; it was based on observations from a 4m class telescope with a limiting *r*-band magnitude of 21.5 and on observations from an 8m class telescope with a limiting *i*-band magnitude of 23.5.

2.2 The PLAsTiCC simulated catalogue

This catalogue arises from a challenge focused on the future use of the LSST¹, by simulating the possible objects on which science will be based. In particular, most of these objects are transients.

LSST will be the largest telescope specialized for the Time Domain Astronomy, whose first light is foreseen in late 2020. Its field of view will be ~ 3.5 degrees (the diameter will be about seven full moons side by side), with a 6.5m effective aperture, a focal ratio of 1.23 and a camera of 3.2 Gigapixel.

¹ <https://www.kaggle.com/c/PLAsTiCC-2018>

Every four nights it will observe the whole sky visible from the Chile (southern hemisphere). Therefore, it will find an unprecedented amount of new transients: Supernovae Ia, Ia-91bg, Iax, II, Ibc, SuperLuminous (SL), Tidal Disruption Events, Kilonova, Active Galactic Nuclei, RR Lyrae, M-dwarf stellar flares, Eclipsing Binary and Pulsating variable stars, μ -lens from single lenses, μ -lens from binary lenses, Intermediate Luminosity Optical Transients, Calcium Rich Transients and Pair Instability Supernovae.

LSST data will be used for studying stars in our Galaxy, understanding how solar systems and galaxies formed and the role played by massive stars in galaxy chemistry as well as measuring the amount of matter in the Universe. PLAsTiCC includes light curves with realistic time-sampling [15], noise properties and realistic astrophysical sources.

Each object has observations in six bands: u (300 \div 400 nm), g (400 \div 600 nm), r (500 \div 700 nm), i (650 \div 850 nm), z (800 \div 950 nm), and y (950 \div 1050 nm). The training set is a mixture of what we can expect to have before LSST, so it is a quite homogeneous ensemble of ~ 8000 objects; the test set, instead, is based on what we expect to have after 3 years of LSST operations and it is formed by $\sim 3,5$ million of objects. The observations are limited in magnitude in single band to 24.5 in the r band and to 27.8 r stacked band (see Figures 2 and 3 for examples of light curves). By combining training and test, we collected the objects per class as listed in Table 2.

Types	Training	Test	Bands	Sampling	%	Amount
SNIa	2313	1659831	u,g,r,i,z,y	uneven	47.57	1662144
SNIax	183	63664	u,g,r,i,z,y	uneven	1.81	63847
SNIa 91bglike	208	40193	u,g,r,i,z,y	uneven	1.15	40401
SNIbc	484	175094	u,g,r,i,z,y	uneven	5.00	175578
SNI	1193	1000150	u,g,r,i,z,y	uneven	28.65	1001343
SLSN I	175	35782	u,g,r,i,z,y	uneven	1.02	35957
AGN	370	101424	u,g,r,i,z,y	uneven	2.89	101794
M-Dwarf	981	93494	u,g,r,i,z,y	uneven	2.68	94475
RR Lyrae	239	197155	u,g,r,i,z,y	uneven	5.63	197394
Mirae	30	1453	u,g,r,i,z,y	uneven	0.04	1483
Eclipse	924	96572	u,g,r,i,z,y	uneven	2.77	97496
KN	100	131	u,g,r,i,z,y	uneven	0.01	231
TDE	495	13555	u,g,r,i,z,y	uneven	0.38	14050
μ Lens	151	1303	u,g,r,i,z,y	uneven	0.04	1454
Other	0	13087	u,g,r,i,z,y	uneven	0.36	13087

Table 2 PLAsTiCC dataset composition.

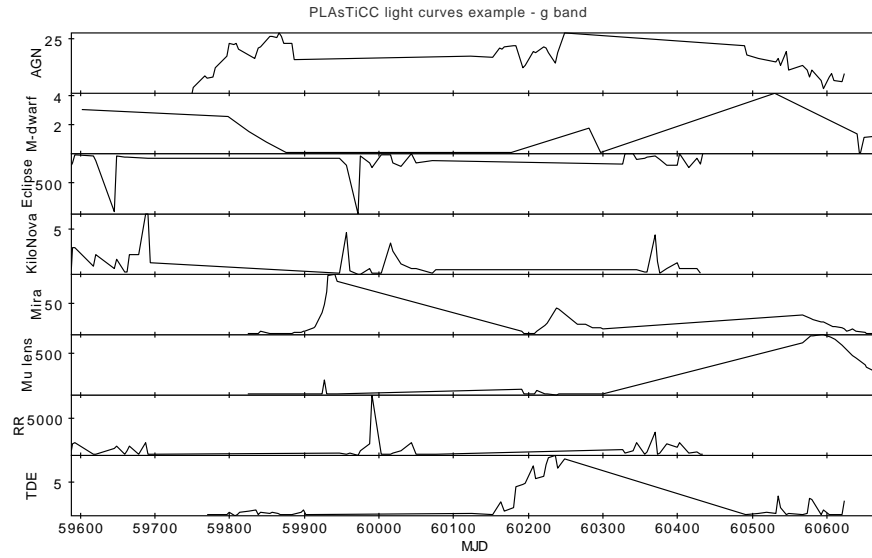


Fig. 2 Examples of PLAsTiCC light curves in g band. From the top to the bottom: 2198(AGN), 2157270(M-Dwarf), 22574(Eclipsing Binary), 139362(Kilonova), 80421(Mirae), 45395(μ -lens), 184176(RR lyrae), 9197(TDE).

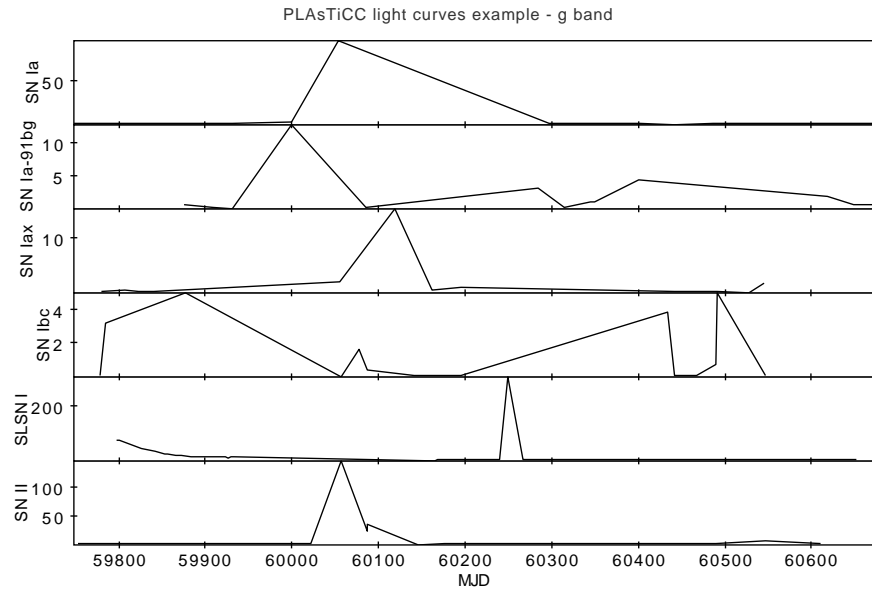


Fig. 3 Examples of PLAsTiCC light curves in g band. From the top to the bottom: 15461391(SNIa), 1143209(SNIa-91bglike), 1019556(SNIax), 1076072(SNIbc), 73610(SLSN I), 1028853(SNII).

2.3 The statistical parameter space

In order to evaluate the classification performances, the light curves of the objects have been subject of a statistical approach, by transforming them into a set of features representing some peculiar characteristics of the astrophysical objects. Within this work we used the following features (already used in a similar task in [18]), resulting from a preliminary mapping of variable object light curves into a statistical parameter space:

- Amplitude (ampl): the arithmetic average between the maximum and the minimum magnitude,

$$ampl = \frac{mag_{max} - mag_{min}}{2} \quad (1)$$

- Beyond1std (b1std): the fraction of photometric points above or under one standard deviation from the weighted average,

$$b1std = P(|mag - \overline{mag}| > \sigma) \quad (2)$$

- Flux Percentage Ratio (fpr): the ratio between two flux percentiles $F_{n,m}$. The flux percentile is defined as the difference between the flux value at percentiles n and m, respectively. For this work, the following fpr values have been used:

$$fpr20 = F_{40,60}/F_{5,95}$$

$$fpr35 = F_{32,5,67,5}/F_{5,95}$$

$$fpr50 = F_{25,75}/F_{5,95}$$

$$fpr65 = F_{17,5,82,5}/F_{5,95}$$

$$fpr80 = F_{10,90}/F_{5,95}$$

- Lomb-Scargle Periodogram (ls): the period obtained by the peak frequency of the Lomb-Scargle periodogram.
- Linear Trend (lt): the slope a of the light curve in the linear fit,

$$mag = a * t + b$$

$$lt = a \quad (3)$$

- Median Absolute Deviation (mad): the median of the deviation of fluxes from the median flux,

$$mad = median_i(|x_i - median_j(x_j)|) \quad (4)$$

- Median Buffer Range Percentage (mbrp): the fraction of data points which are within 10% of the median flux,

$$mbrp = P(|x_i - median_j(x_j)| < 0.1 * median_j(x_j)) \quad (5)$$

- Magnitude Ratio (mr): an index to see if the majority of data points are above or below the median of the magnitudes,

$$mr = P(mag > median(mag)) \quad (6)$$

- Maximum Slope (ms): the maximum difference obtained measuring magnitudes at successive epochs,

$$ms = \max\left(\left|\frac{mag_{i+1} - mag_i}{(t_{i+1} - t_i)}\right|\right) = \frac{\Delta mag}{\Delta t} \quad (7)$$

- Percent Difference Flux Percentile (pdfp): the difference between the fifth and the 95th percentile flux, converted in magnitudes, divided by the median flux,

$$pdfp = \frac{(mag_{95} - mag_5)}{median(mag)} \quad (8)$$

- Pair Slope Trend (pst): the percentage of the last 30 couples of consecutive measures of fluxes that show a positive slope,

$$pst = P(x_{i+1} - x_i > 0, i = n - 30, \dots, n) \quad (9)$$

- R Cor Bor (rcb): the fraction of magnitudes that is above 1.5 magnitudes with respect to the median,

$$rcb = P(mag > (median(mag) + 1.5)) \quad (10)$$

- Small Kurtosis (kurt): the ratio between the 4th order momentum and the square of the variance. For small kurtosis it is intended the kurtosis on a small number of epochs,

$$kurt = \frac{\mu_4}{\sigma^2} \quad (11)$$

- Skewness (skew): the ratio between the 3rd order momentum and the variance to the third power,

$$skew = \frac{\mu_3}{\sigma^3} \quad (12)$$

- Standard deviation (std): the standard deviation of the flux.

3 Machine Learning models

A classifier can be used as a descriptive model to distinguish among objects of different classes, and as a predictive model to predict the class label of input patterns. Classification techniques work better for predicting or describing data sets with binary or nominal categories. Each technique uses a different learning algorithm to find a model that fits the relationship between the feature set and class labels

of the input data. The goal of the learning algorithm is to build models with good generalization capability. The typical approach of machine learning models is to randomly shuffle and split the given input dataset with known assigned class labels into three subsets: training, validation and blind test sets. The validation set can be used to validate the learning process, while the test set is used blindly to verify the trained model performance and generalization capabilities. In the following sections we briefly introduce the methods used to perform the classification experiments, together with the statistical estimators adopted to evaluate their performances.

3.1 The Random Forest classifier

A Random Forest (RF, [8]) is a classifier consisting of a collection of tree-structured classifiers $\{h(x, \Theta_k), k = 1, \dots\}$ where the $\{\Theta_k\}$ are independent identically distributed random vectors and each tree casts a unit vote for the most popular class at input x [19]. The generalization error for this algorithm depends on the strength of single trees and from their correlations through the raw margin functions. The upper bound, instead, tell us that smaller the ratio of those quantities, better the RF performance. To improve the model accuracy by keeping trees strength, the correlation between trees is decreased and bagging with a random selection of features is adopted. Bagging or Bootstrap Aggregating, is a method designed to improve the stability and accuracy of machine learning algorithms. It also reduce variance and minimizes the risk of overfitting. Given a training set of size n , bagging generates m new training sets, each of size p , by sampling from the original one uniformly and with replacement. This kind of sampling is known as a bootstrap sample. The m models are fitted using the m bootstrap samples and combined by averaging the output (for regression) or voting (for classification). Bagging is useful because, in addition to improving accuracy when using random features, it provides an estimate of the generalized error of the set of trees and the strength and correlation of trees. The estimation is done out-of-bag. Out-of-bag means that the error estimate of each pair (x,y) is made on all those bagging datasets that do not contain that given pair.

3.2 The Nadam, RMSProp and Adadelata classifiers

The simplest optimization algorithm is the *Gradient Descent*, in which the gradient of the function to be minimized is calculated. This depends on the parameter θ_{t-1} . Only a portion of the gradient is used to update the parameters; this portion is given by the parameter η :

$$\begin{cases} g_t \leftarrow \nabla_{\theta_{t-1}} f(\theta_{t-1} - \eta \mu m_{t-1}) \\ m_t \leftarrow \mu m_{t-1} + g_t \\ \theta_t \leftarrow \theta_{t-1} - \eta m_t \end{cases}$$

where m is the so-called *momentum vector*, used to accelerate the update of the learning function, while μ is the decay constant. These two terms increase the speed of gradient decreasing in the direction where the gradient tends to remain constant, while reducing it where the gradient tends to oscillate.

Nadam is a modified version of the Adam algorithm, based on the combination between the momentum implementation and the L_2 normalization. This type of normalization changes the η member, dividing it by the L_2 norm of all previous gradients.

Adadelta is a variant that tries to reduce the aggressive, monotonically decreasing learning rate. In fact, instead of accumulating all past squared gradients, it restricts the window of accumulated past gradients to some fixed size w . This has the advantage of compensating for the speeds along the different dimensions by stabilizing the model on common features and allowing the rare ones to emerge. A problem of this algorithm comes from the norm vector that could become so large to stop the training, preventing the model from reaching the local minimum. This problem is solved by RMSProp, a L_2 normalization based algorithm, which replaces the sum of n_t with a decaying mean, characterized by a constant value ν . This allows the model to avoid any stop of the learning process. For a detailed description of these models, see [9].

3.3 Parameter Space exploration

The choice of an optimal set of features is connected to the concept of feature importance, based on the measure of a feature's relevance [11]. Formally, the importance or relevance of a feature is its percentage of informative contribution to a learning system. We approached the feature selection task in terms of the *all-relevant* feature selection, able to extract the most complete parameter space, i.e. all features considered relevant for the solution to the problem. This is appropriate for problems with highly correlated features, as these features will contain nearly the same information. With a minimal-optimal feature selection, choosing any one of them (which could happen at random if they are perfectly correlated), means that the rest will never be selected. The method Φ LAB, deeply discussed in [11], includes properties of both embedded and wrappers categories of feature selection to optimize the parameter space, by solving the *all-relevant* feature selection problem, thus indirectly improving the physical knowledge about the problem domain.

3.4 Classification statistics

In this work, the performance of the classification models is based on some statistical estimators, extracted from a matrix known as *confusion matrix* [20].

		Predicted	
		P=0	N=1
Target	p=0	a_{00}	a_{10}
	n=1	a_{01}	a_{11}

Table 3 Example of a binary confusion matrix.

The example shown in Table 3 is a confusion matrix for a binary classification. Each entry a_{ij} in this table is the number of records from class i predicted to be of class j . The numbers a_{00} and a_{11} show correct classified records. The a_{01} records named *False Positive* indicate wrong records classified in class 0, when their correct classification was class 1; instead, a_{10} named *False Negative* show the records classified in class 1 but belonging to class 0. The total number of correct predictions is $a_{11} + a_{00}$, and the total number of wrong ones is $a_{10} + a_{01}$. For a better comparison between different models, summarizing the results through a confusion matrix is the common way. We can do this using a *performance metric*, such as *accuracy*, defined as follows:

$$Accuracy = \frac{a_{00} + a_{11}}{a_{00} + a_{11} + a_{01} + a_{10}}$$

A highest accuracy is the target of every classifier. Other important statistical estimators, for a better understanding of the results for each class, are:

$$Purity = \frac{TruePositive}{TruePositive + FalsePositive}$$

$$Completeness = \frac{TruePositive}{TruePositive + FalseNegative}$$

$$Contamination = 1 - Purity = \frac{FalsePositive}{TruePositive + FalsePositive}$$

$$F1_{Score} = \frac{2}{(Purity)^{-1} + (Completeness)^{-1}}$$

Purity of a class is the percentage of correctly classified objects in that class, divided by the total classified objects in that class. Also named as precision of a class.

Completeness of a class is the percentage of the correctly classified objects in that class divided by the total amount of objects belonging to that class. Also named as recall of a class.

Contamination of a class is the dual measure of purity.

F1-Score of a class is the harmonic mean between purity and completeness of that class and it is a measure of the average trade-off between purity and completeness.

4 Experiments

In order to pursue the main goal of the present work, related to a deep analysis of SNe in terms of their classification and characterization of the parameter space required to recognize their different types, we relied on the two simulation datasets, one in particular developed and specialized within the LSST project (see Sections 2.1 and 2.2). We preferred a statistical approach, by mapping the light curves into a set of statistical features. The classification with statistical data have been performed through the comparison of different types of classifiers, respectively, Nadam, RMSProp, Adadelta and Random Forest.

A data pre-processing phase was carried out on the PLAsTiCC dataset, based on a pruning on the flux and related error, in order to reduce the amount of negative fluxes present within data, which could affect the learning capability of the machine learning models. On the SNPhotCC dataset, both the errors in the flux and the quantity of negative fluxes were such that it was not deemed necessary to perform the pruning. The curves in the PLAsTiCC dataset were selected in successive steps so as to minimize the presence of negative fluxes, reaching, where possible, a subset of about 35,000 light curves per type. In the SNPhotCC dataset, on the other hand, all the given 5088 SN-Ia curves were selected and the type II curves were reduced so as to balance the classes; the other types of SNe have been discarded, due to their negligible amount available.

The sequence of classification experiments followed an incremental complexity, starting from the most simple exercise on the PLAsTiCC dataset, i.e. the separation between periodic and non-periodic objects (*P Vs NP*), expected to be well classified due to their very different features within any parameter space. In terms of initial minimization of negative fluxes, it was decided to apply the following replacement: for each class of objects, the observations related to the same day were grouped, by taking the least positive flux value. This value has been replaced to all the negative fluxes of that day.

As expected, the classifiers revealed a high capability to disentangle periodic from non-periodic objects. Therefore, in all further experiments we excluded periodic sources, by focusing the exclusive attention to variable objects, increasing the complexity of classification, by considering different sub-classes of transients and evaluating the performances of the selected machine learning classifiers.

The next step was, in fact, to recognize the SNe from all the other non-periodic objects available in the dataset (*SNe Vs All*). But, preliminarily, we tested different methods for replacing the negative fluxes. For instance, in addition to the first mentioned method (e.g. minimum positive flux extracted from observations within the same day), a second method was chosen, in which negative fluxes were replaced by the constant number 0.001, considered as the absolute minimum flux emitted by the sources. We tried also a third method, in which the negative fluxes were simply excluded from the input dataset, without any replacement. In theory, such third method was considered the worst case, since it would cause a drastic reduction of the light curve sample available. As we will show, the second method (the constant

minimum flux value), obtained the best classification performances for all classifiers. Therefore, it was used as the reference for all further classification experiments.

The subsequent experiments concerned some fine classifications of most interesting SNe types, starting from the classic case of *SNIa Vs SNI* types, followed by a mix of *SNIa Vs Superluminous SNe I (SNIa Vs SL-I)*, concluding with the most complex case, based on the multi-class experiment, in which we tried to simultaneously classify all six different types of SNe (*six-class SNe*).

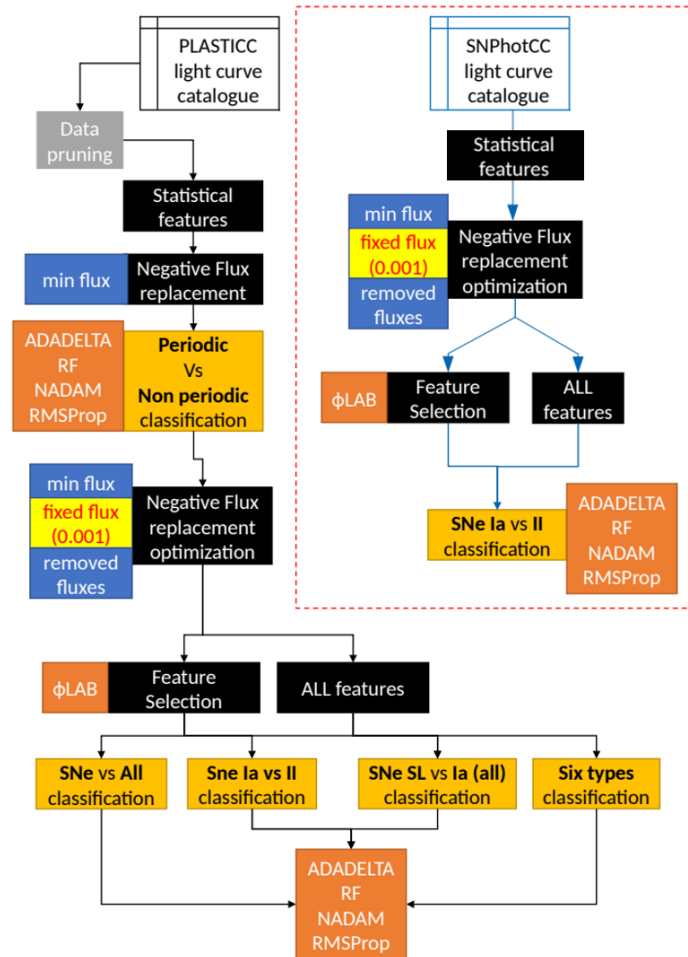


Fig. 4 Summary of the procedure designed and followed along the experiments.

Besides the negative flux replacement, we investigated also the feature selection problem, in order to identify the most significant parameter space able to recognize different types of SNe. After the selection process we verified that such reduced

amount of data dimensions could maintain sufficiently high the classification performances. We tried also to maintain uniform the number of features among the different use cases, although respecting their statistical importance, exploring the possibility to find a common parameter space, suitable for all classification cases.

The *SNIa Vs SNI* use case was also performed on the SNPhotCC dataset, since this dataset was composed almost exclusively by such two types of SNe. The results were then compared with those performed on the PLAsTiCC dataset, deprived of the u and y bands for uniformity with the SNPhotCC dataset bands, in order to maximize the fair comparison.

In summary, in this work five series of experiments were performed on the PLAsTiCC dataset and one on the SNPhotCC dataset. Such experiments were chosen hierarchically and considering the most important goal of this work, i.e. the fine classification of SNe types. An overview of the followed procedure is shown in Fig. 4.

4.1 Data pre-processing

From the whole PLAsTiCC dataset a maximum of 200,000 objects per class was randomly extracted (whenever possible). For each class, a pruning in flux and its error was performed. While, no any pruning was done on the SNPhotCC dataset. The Table 4 shows the limits derived from pruning.

After this first skimming, the amount of objects for the various classes was reduced to a maximum of about 35,000 curves. The reduction for classes with more than 35K objects was driven by the choice of the curves with the least number of observations with negative fluxes and with at least 6 observations per band.

Due to the residual presence of negative fluxes, we started their handling by trying the following replacement method. By considering all the curves of a class, we checked all the observations of a given day. If in that day there was a negative or zero flux, then it was replaced with the lowest positive flux present. Else if only negative fluxes were present, they were replaced with the lowest positive flux of the previous day. This replacement has been applied to every day, for all curves and for all classes. An example of the replacing method is shown in Table 5.

Since 19 features have been chosen for our statistical approach, by considering 6 bands in PLAsTiCC, a total of 114 features composed the original parameter space.

After the composition of statistical datasets, some light curves included some missing entries, or *NaN* (Not-a-Number), causing the exclusion of those objects from the datasets, due to their unpredictable impact on the training of classifiers. The total amount of light curves per class is reported in Table 6.

Object	Band	Flux	Flux Error	Object	Band	Flux	Flux Error
AGN	u	> -50	<160	M-Dwarf	u	>-60	<300
	g,r	>-50	<160		g,r	>-60	<100
	i,z	>-50	<160		i,z	>-60	<80
	y	>-50	<160		y	>-60	<180
E. Binary	u	>-200	<800	Kilonova	u	>-10	<60
	g	>-800	<800		g	>-10	<20
	r	>-900	<800		r	>-10	<20
	i	>-800	<800		i	>-10	<25
	z	>-1100	<800		z	>-20	<40
y	>-800	<650	y	>-30	<70		
Mirae	u	>-30	<2500	μ Lens	u	>-40	<1700
	g	>-20	<800		g	>-20	<250
	r	>-50	<900		r	>-30	<400
	i	>-1200	<1700		i	>-40	<300
	z	>-8000	<3000		z	>-60	<400
y	>-11000	<3300	y	>-90	<500		
RR Lyrae	u	>-1300	<1500	SN Ia	u	>-50	<1350
	g	>-6000	<1500		g	>-20	<500
	r	>-6000	<1500		r	>-20	<400
	i	>-4500	<1500		i	>-40	<170
	z	>-4500	<1200		z	>-60	<200
y	>-5500	<1200	y	>-100	<300		
SN Iax	u	>-30	<550	SN Ia91bg	u	>-30	<800
	g	>-10	<150		g	>-20	<200
	r	>-20	<150		r	>-20	<200
	i	>-30	<100		i	>-30	<150
	z	>-50	<125		z	>-40	<150
y	>-90	<200	y	>-90	<325		
SN Ibc	u	>-50	<800	SN II	u	>-40	<200
	g	>-20	<200		g	>-20	<100
	r	>-20	<150		r	>-20	<100
	i	>-30	<100		i	>-30	<100
	z	>-60	<125		z	>-60	<100
y	>-110	<350	y	>-110	<150		
SL SN I	u	>-30	<1000	TDE	u	>-20	<200
	g	>-10	<150		g	>-10	<50
	r	>-15	<125		r	>-10	<50
	i	>-20	<100		i	>-20	<50
	z	>-40	<100		z	>-30	<75
y	>-70	<175	y	>-60	<150		

Table 4 Table of values retained after data pruning on the classes of PLAsTiCC dataset.

4.2 Periodic Vs Non Periodic

This was the first classification experiment, performed only on PLAsTiCC simulation. Having no need, at this level, to optimize the treatment of negative fluxes, we used only the method previously described (Sec. 4.1). We had RR lyrae, Mirae variables and Eclipsing Binaries in the periodic class (P) and all the others in the non periodic (NP) class. To balance the classes we excluded some objects in the second

ID	MJD	Flux	
		Before	After
1	59820.0015	-25.154862	0.284215
2	59820.0238	15.458932	15.458932
3	59820.1234	-5.848961	0.284215
4	59820.4451	-20.548951	0.284215
5	59820.8251	0.284215	0.284215
6	59820.0234	-9.542318	0.284215
7	59820.6234	10.854215	10.854215

Table 5 Example of the negative fluxes replacement within the PLAsTiCC catalogue.

Dataset	Object	Curves	Object	Curves
PLAsTiCC	AGN	34666	E. Binary	34484
	Kilonova	232	M-Dwarf	34849
	Mirae	1154	μ Lens	1187
	RR Lyrae	32698	SN Ia	34953
	SN Iax	34977	SN Ia 91bg	34923
	SN Ibc	34932	SN II	34828
	SL SN I	34959	TDE	14023
	Total objects		361711	
SNPhotCC	SN Ia	5088	SN II	12027
	Total objects		17115	

Table 6 Summary of the light curves composing the simulated datasets.

class, as shown in Table 7. The random partitioning percentage between training and test sets was fixed, respectively, to 80% and 20%.

Object	Number of curves		Object	Number of curves	
	Training	Test		Training	Test
RR Lyrae	26158	6540	Kilonova	187	46
E. Binary	27587	6897	M-Dwarf	6001	1501
Mirae	923	231	μ Lens	950	238
AGN	6001	1501	SN Ia	6001	1501
SN Iax	6001	1501	SN Ia 91bg	6001	1501
SN Ibc	6001	1501	SN II	6001	1501
SL SN I	6001	1501	TDE	6001	1501
Total P Training		54668	Total NP Training		55146
Total P Test		13668	Total NP Test		13793

Table 7 Summary of the sources belonging to the PLAsTiCC dataset in the P (periodic class) Vs NP (non periodic class) use case divided in training (80%) and test (20%) sets.

This series of experiments, as expected, being the simplest given the intrinsic difference of the objects involved, did not reveal any surprise. All estimators showed a great efficiency to recognize periodic objects from the variables (non periodic) ones.

%	type	RF	Nadam	RMSProp	Adadelta
Accuracy	-	99	97	98	96
Purity	NP	99	97	99	95
	P	99	98	98	97
Completeness	NP	99	98	98	97
	P	99	97	99	95
F1 Score	NP	99	98	98	96
	P	99	97	98	96

Table 8 Summary of the best results (in percentages) for the 4 classifiers in the classification experiment P Vs NP . For Nadam, RMSProp and Adadelta models, a decay value of 10^{-5} and a learning rate of 0.0005 were assigned.

4.3 Handling of negative fluxes

In both simulated catalogues, as introduced in Sec. 4, the presence of negative fluxes required an investigation on how to replace them in order to minimize their negative impact on the learning efficiency of machine learning models. Therefore, it was decided to approach this problem in three ways.

The first (named as $M1$) was to replace their value as introduced in Sec. 4 (and preliminarily used for the Periodic Vs Non Periodic classification experiment, described in Sec. 4.2): for each class of objects, the observations related to the same day were grouped, by taking the least positive flux value. This value has been replaced to all the negative fluxes of that day.

The second approach (named as $M2$) was to replace the negative fluxes with a constant value of 0.001, considered as the minimum flux emitted by the sources.

The third solution ($M3$) consisted into the total rejection of negative fluxes from the dataset, without any replacement.

The impact on classification accuracy has been analyzed by comparing the three solutions in the SNe Vs All (the class All includes the rest of transient types) classification experiment on the Plasticc dataset and the $SNIa$ Vs SNI experiment on the SNPhotCC dataset. In both cases, the data have been treated with the three replacement types, producing different amount of objects per class. The entire composition of the datasets for the three methods is shown in Table 9, while the composition of the classes of SN, All, SNIa and SNI are shown in Table 10.

The results of the two experiments are shown, respectively, in Tables 11 and 12. The results indicated that, on average, in the case of the PLAsTiCC dataset, the second method ($M2$) obtained a better accuracy, with some exception in favor of $M3$. In the case of SNPhotCC dataset, on the other hand, $M2$ and $M3$ resulted more close in terms of classification efficiency. Therefore, since we were mostly interested to directly compare the classification performances between the two datasets, by considering also the drastic reduction of available sources using the $M3$ method, we definitely selected and applied the $M2$ to both datasets.

	Object	Number of curves			Object	Number of curves		
		<i>M1</i>	<i>M2</i>	<i>M3</i>		<i>M1</i>	<i>M2</i>	<i>M3</i>
PLAsTiCC	AGN	34666	34666	34082	Kilonova	232	232	229
	μ Lens	1187	1187	1144	M-Dwarf	34849	34849	34191
	SN Ia	34953	34891	34423	SL SN I	34959	34959	34750
	SN Iax	34977	34977	34680	SN Ia 91bg	34923	34923	34559
	SN Ibc	34932	34932	34437	SN II	34828	34771	34393
	TDE	14023	14023	13985				
Total objects <i>M1</i> :		294529	Total objects <i>M2</i> :	294410	Total objects <i>M3</i> :	290873		
SNPhotCC	SN Ia	5088	5088	5086	SN II	5088	5088	5077
Total objects <i>M1</i> :		10176	Total objects <i>M2</i> :	10176	Total objects <i>M3</i> :	10163		

Table 9 Summary of sources of datasets for each replacing method adopted for negative fluxes.

	Object	<i>M1</i>		<i>M2</i>		<i>M3</i>	
		Training	Test	Training	Test	Training	Test
PLAsTiCC	AGN	27732	6934	27732	6934	27266	6816
	Kilonova	186	46	186	46	183	46
	μ Lens	949	238	949	238	915	229
	M-Dwarf	27879	6970	27879	6970	27353	6838
	SN Ia	12001	3001	11975	2994	11802	2954
	SL SN I	12001	3001	12001	3001	11935	2979
	SN Iax	12001	3001	12001	3001	11900	2976
	SN Ia 91bg	12001	3001	12001	3001	11866	2975
	SN Ibc	12001	3001	12001	3001	11828	2951
	SN II	12001	3001	11983	2992	11835	2970
TDE	11218	2805	11218	2805	11188	2797	
Total SN	72006	18006	71962	17990	71166	17805	
Total All	67964	16993	67964	16993	66905	16726	
SNPhotCC	SN Ia	4071	1017	4071	1017	4062	1016
	SN II	4071	1017	4071	1017	4070	1015

Table 10 Summary of sources of training and test sets for each negative flux replacing method.

4.4 Optimization of the Parameter Space for transients

After choosing how to handle the negative fluxes, we investigated the statistical parameter space (PS) of the two simulated datasets, in order to explore the possibility to reduce the dimensionality of the classification problem (feature selection) and to analyze the impact of the resulting optimized PS on the classification efficiency for each particular type of classes involved in all cases, as well as the possibility to find a common set of relevant features, suitable to separate different types of transients. We applied the Φ LAB algorithm, introduced in Sec. 3.3, to both datasets in various classification use cases (except the preliminary experiment *P Vs NP*), obtaining an optimized parameter space for each of them. The analysis of feature commonalities among all classification experiments is shown in Fig. 5. In particular, the feature selection of the *SN Ia Vs SN II* use case has been done on the PLAsTiCC dataset

Dataset	Use case	Algorithm	Class	Estimator	$M1$	$M2$	$M3$	
PLAsTiCC <i>SNe Vs All</i>	RF	SN		Purity	86	91	85	
			Completeness	94	93	91		
			F1-score	90	92	88		
		All		Purity	93	92	90	
			Completeness	83	90	83		
			F1-score	88	91	86		
		Nadam	SN		Purity	77	84	83
				Completeness	82	78	85	
				F1-score	79	81	84	
			All		Purity	80	78	84
				Completeness	73	85	82	
				F1-score	76	81	83	
	RMSProp	SN		Purity	85	89	87	
			Completeness	83	89	91		
			F1-score	84	89	89		
		All		Purity	83	88	90	
			Completeness	85	89	86		
			F1-score	84	88	88		
	Adadelta	SN		Purity	80	85	85	
			Completeness	84	86	87		
			F1-score	82	86	86		
		All		Purity	82	85	86	
			Completeness	78	84	84		
			F1-score	80	85	85		

Table 11 Comparison among the three replacing methods for negative fluxes on the PLAsTiCC dataset in the classification case *SNe Vs All*. For Nadam, RMSProp and Adadelta a learning rate of 0.001 and a decay value of 10^{-5} were chosen. The statistics are expressed in percentages.

deprived of the u and y bands, for uniformity with the SNPhotCC dataset in terms of direct comparison.

From the analysis of the histogram of Fig. 5 it was possible to extract a common optimized parameter space, composed by relevant features with higher percentage of common occurrences among various classification use cases (the cumulative measurement process is explained in the caption of the Fig. 5). The extraction was done trying also to balance the different amount of relevant features provided by Φ LAB in every classification case with their percentage of commonality among different cases, with the aim at extracting the same number of relevant features in all cases. The best compromise found is reported in Table 13 and corresponds to 78 extracted features (on a total of 114) suitable for the six-band cases (*ugrizy* in PLAsTiCC) and 52 (on a total of 76) for the four-band cases (*griz* in SNPhotCC). These two resulting optimized (reduced) parameter spaces have been used in the classification cases described in the next sections, each time by comparing the classification efficiency between the complete and the reduced parameter spaces.

By looking at the optimized parameter spaces obtained (Fig. 5), extremely interesting is the presence of some common features among the various classification cases. In particular, the Amplitude (*ampl*) shows a crucial role for the classification of various SNe types. Also important is the Standard Deviation (*std*), which reaches

Dataset	Use case	Algorithm	Class	Estimator	M1	M2	M3
SNPhotCC	<i>SN Ia Vs SN II</i>	RF	SN Ia	Purity	91	95	91
				Completeness	94	97	93
				F1-score	93	96	92
			SN II	Purity	94	97	93
				Completeness	91	95	91
				F1-score	92	96	92
		Nadam	SN Ia	Purity	86	91	92
				Completeness	92	92	94
				F1-score	89	92	93
			SN II	Purity	91	92	94
				Completeness	86	91	92
				F1-score	88	91	93
		RMSProp	SN Ia	Purity	91	92	93
				Completeness	93	96	94
				F1-score	92	94	94
			SN II	Purity	93	96	94
				Completeness	91	92	93
				F1-score	92	94	94
		Adadelta	SN Ia	Purity	89	86	92
				Completeness	92	88	92
				F1-score	91	87	92
			SN II	Purity	92	88	92
				Completeness	89	85	92
				F1-score	90	87	92

Table 12 Comparison among the three replacing methods for negative fluxes on the SNPhotCC dataset in the classification case *SN Ia Vs SN II*. For Nadam, RMSProp and Adadelta a learning rate of 0.001 and a decay value of 10^{-5} were chosen. The statistics are expressed in percentages.

Feature	[<i>SNe Vs All</i>]	[<i>SN Ia Vs SN II</i>]	[<i>SN Ia Vs SL-I</i>]	[<i>six-class SNe</i>]	[<i>SN Ia Vs SN II</i>]
	PLAsTiCC				SNPhotCC
ampl_{band}	x	x	x	x	x
pdf_{band}	x	x	x		x
ms_{band}				x	
mad_{band}	x	x	x	x	x
std_{band}	x	x	x	x	x
skew_{band}	x	x	x	x	x
fprXX_{band}	x	x	x	x	x
kurt_{band}	x	x	x	x	x
ls_{band}	x	x	x	x	x
lt_{band}	x	x	x	x	x
Totals	PLAsTiCC: 78			SNPhotCC: 52	

Table 13 Summary of the resulting common optimized parameter spaces from the analysis of the feature selections. Each feature listed is intended to include all its available bands. First four use cases (columns 2 to 5) refer to the classification cases approached on PLAsTiCC with such optimized PS in six bands (*ugrizy*), while last column is referred to the classification experiment done with SNPhotCC in four bands (*griz*). For PLAsTiCC the optimized PS include 78 features, while SNPhotCC is composed by 52. Take into account that the feature fprXX_{band} includes 5 different types per band group (See Sec. 2.3 for details).

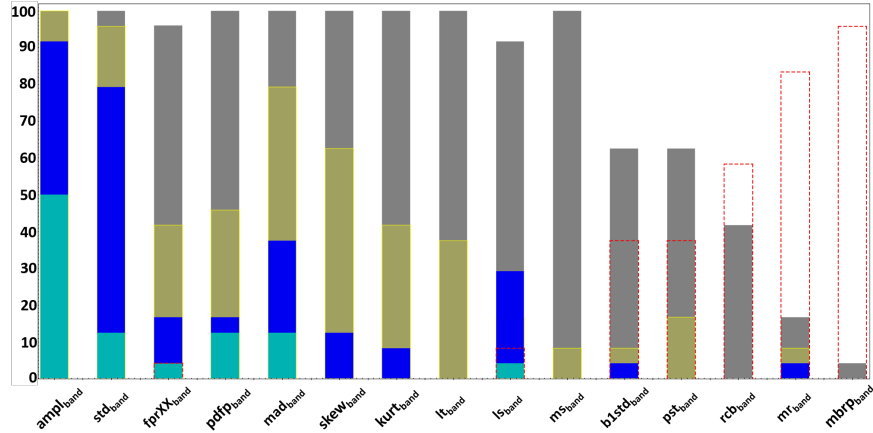


Fig. 5 Cumulative statistical analysis of the feature selection performed with the method Φ LAB on different use cases. The results include the four classification cases on PLAsTiCC (*SN Vs All*, *SN Ia Vs SNI*, *SN Ia Vs SL-I*, *six-class SNe*) and the single case *SN Ia Vs SNI* on SNPhotCC. The indicated features are grouped per statistical type, including all their available bands. After having calculated the various feature rankings for each classification use case with Φ LAB, ordered by decreasing importance, the vertical bars shown in the histogram represent the percentage of common occurrences of each feature type, among various classification use cases, within, respectively, the first 25% (cyan), 50% (blue), 75% (yellow) and 100% (gray) of feature rankings. While dotted red bars indicate the percentage of common occurrences of rejection among various feature rankings.

79.2% of common occurrences. Equally interesting appears the high percentage of common rejections of Median Buffer Range Percentage (*mbrp*), Magnitude Ratio (*mr*) and R Cor Bor (*rcb*). Within most of the light curves of the datasets used, the average value of the *mbrp*, which is the percentage of points in an interval of 10% of the median flux, is very high. This shows that most of the light curves are relatively contained within the flux extension. The *mr* feature, the percentage of points above the median magnitude, has always values greater than 40%, with a standard deviation of a lower order of magnitude, except in the case of the *six-class SNe* problem, in which the standard deviation is comparable with the *mr* value. This shows that most of the light curves are basically symmetrical in magnitude. Finally, the *rcb* has an average value of about 30% with a comparable standard deviation. Therefore, it ranges over the whole spectrum of possible values without any class distinction.

The *ampl*, which from a physical point of view represents the half-amplitude, in magnitude, of the light curves, is the most important feature in all use cases and it is related to the different distribution of objects in the classes. In the *SNe Vs All* use case, the class of SNe shows a bi-modal distribution, while the class *All* shows an alternation between bi-modal and uni-modal distributions, with different peaks from the SNe distributions. In the *SN Ia Vs SL-I* use case, the SNe Ia have a bi-modal distribution, unlike the SL-I type, which instead is uni-modal. The *six-class SNe* use case shows that the SNe Ia have a similar peak w.r.t. the sub-types *Iax*, *Iabg91*, *SL* and the *Ibc*. The SNe II instead, show an unexpected shape similarity with the SNe

Ia in the PLAsTiCC simulation, and this should explain a classification efficiency in the *SNIa Vs SNIi* case smaller than what obtained on the SNPhotCC data (see Sec. 4.6).

The *std*, the deviation from the mean flux, has the same trend of the *ampl*, with bi-modal and uni-modal distributions and with peaks at different values.

The *fpr*, the flux percentage ratio, related to the sampling of the light curve assuming a relevance with the higher flux values, shows that, in the *SNe Vs All* case and with the *griz* bands, there are two distributions with distinguishable peaks. In the *six-class SNe* case, the *riz* bands, with the wider flux ratios, contribute to solve the envelope of the 6 classes. In the *SNIa Vs SL-I* case, the different distributions can be particularly identified in the *rizy* bands, again in the broader flux ratios such as 50, 65 and 80. Finally, in the *SNIa Vs SNIi* problem the distinction is more complex and only in few *riz* band cases it is possible to see the two different distributions.

In the other relevant features shown in Fig. 5, we do not infer distinct distributions in the various use cases, but only different fluctuations around the same distribution. This means that all the curves of all the classes share, more or less, the same distribution w.r.t. the flatness of the curve (*kurt*), the symmetry of the curve (*skew*), the slope deriving from the linear fit (*lt*), the period obtained from the peak frequency of the Lomb Scargle Periodogram (*ls*), the ratio of difference between percentiles and the median (*pdfp*) and finally the median of deviations from the median (*mad*). Since these features have proved to be highly relevant, this implies that those fluctuations in the class distributions contribute substantially to the classification of different types of SNe. Finally, in the *six-class SNe* problem, another feature appears relevant, which is the maximum difference in magnitude between two successive epochs (*ms*), providing, slightly in the *u* band and in a more consistent way in the *y* one, fluctuations suitable in principle for the resolution of the more complex classification.

4.5 Supernovae versus All

In this use case we had SNe type Ia, Iax, Ia 91bg-like, Ibc, II and SL-I within the *SNe* class and all the other object types, except the excluded periodic ones, in the *All* class. We performed the experiments on the PLAsTiCC dataset with the 4 classifiers using, respectively, the entire set of statistical features available (114) and with the optimized parameter space (78). The amount of objects for each type included in the two classes is shown in Table 14.

Among Nadam, RMSProp and Adadelta, the best performances were obtained with the RMSProp in both cases (whole and optimized parameter spaces). While Random Forest reached the best classification performances. The statistical results are shown in Table 15.

Type	Training	Test
SN Ia	11975	2994
SN Iax	12001	3001
SN Ia91bg	12001	3001
SN Ibc	12001	3001
SN II	11983	2992
SL SN I	12001	3001
Kilonova	186	46
M-Dwarf	27879	6970
μ Lens	949	238
TDE	11218	2805
AGN	27732	6934
Total SN	71962	17990
Total All	67964	16993

Table 14 Summary of the objects belonging to the PLAsTiCC dataset, used for the *SNe Vs All* experiment, randomly partitioned in training (80%) and test (20%) sets.

Features	Random Forest Nadam RMSProp Adadelata								
	All	78	All	78	All	78	All	78	
% Accuracy	-	92	92	85	86	90	90	86	85
% Purity	SN	91	91	85	86	91	91	86	84
	All	92	92	85	86	89	90	86	86
% Completeness	SN	93	93	86	87	90	90	87	87
	All	90	90	84	85	90	90	85	83
% F1 Score	SN	92	92	86	87	90	87	87	86
	All	91	91	84	86	90	86	86	84

Table 15 Summary of the statistical results for the 4 classifiers with, respectively, all the features and the 78 selected. For Nadam, RMSProp and Adadelata, the values of 10^{-5} and 0.0005 were assigned to the decay and learning rate hyper-parameters, respectively.

4.6 Supernovae Ia versus II

In this experiment we considered only SNe of type Ia and II. In this case it was possible to use both SNPhotCC and PLAsTiCC datasets, since in the case of SNPhotCC, these two types of SN were available. The amount of objects used is shown in Table 16.

Dataset	Type	Number of curves	
		Training	Test
PLAsTiCC	SN Ia	27964	6990
	SN II	27983	6966
	Total	55947	13956
SNPhotCC	SN Ia	4071	1017
	SN II	4071	1017
	Total	8142	2034

Table 16 Summary of the objects belonging to the datasets used for the *SNIa Vs SNIi* experiment on PLAsTiCC and SNPhotCC, randomly partitioned in training (80%) and test (20%) sets.

We performed the experiment with the 4 classifiers using, respectively, all the features and the amounts related to the two optimized feature sets, respectively, 78 for PLAsTiCC and 52 for SNPhotCC. For a direct comparison between the SNPhotCC and PLAsTiCC datasets, we also considered a reduced version of the PLAsTiCC dataset, by excluding the u and y bands for uniformity with the SNPhotCC catalogue in terms of bands available. The statistical results are reported in Table 17.

	Random Forest				Nadam				RMSProp				Adadelata								
	PLA		SNP		PLA		SNP		PLA		SNP		PLA		SNP						
Bands used	6	6	4	4	4	6	6	4	4	4	6	6	4	4	4	6	6	4	4	4	
Features	All	78	52	All	52	All	78	52	All	52	All	78	52	All	52	All	78	52	All	52	
% Accuracy	-	78	79	78	96	96	71	72	71	93	94	76	76	78	94	96	74	74	73	90	95
% Purity	Ia	76	76	76	95	95	70	70	69	90	92	74	74	75	93	94	72	73	72	89	93
	II	81	81	80	97	97	72	73	74	95	96	78	78	80	95	98	75	74	75	92	96
% Completeness	Ia	82	83	82	97	97	75	76	77	96	96	79	80	82	95	98	76	75	77	92	96
	II	74	74	74	95	95	67	67	65	89	92	73	71	73	93	93	71	72	70	88	93
% F1 Score	Ia	79	79	79	96	96	72	73	73	93	94	77	77	79	94	96	74	74	74	90	95
	II	77	78	77	96	96	70	70	69	92	94	75	74	76	94	95	73	73	72	90	95

Table 17 Summary of the statistical results for the 4 classifiers in the *SNIa Vs SNI* experiment. For each classifier it is reported the statistics related to the PLAsTiCC (PLA columns) and SNPhotCC (SNP columns) datasets. In the case of PLAsTiCC, the columns are related to the whole original feature space (All) and the optimized one (78) using 6 bands (*ugrizy*), together with the reduced feature space (52) using 4 bands (*griz*) for a direct comparison with the corresponding optimized parameter space obtained on SNPhotCC. For Nadam, RMSProp and Adadelata, the values of 10^{-5} and 0.0005 were assigned to, respectively, the decay and learning rate hyper-parameters, in the cases of 78 features. While 10^{-5} and 0.001 values have been assigned for the cases with 52 features.

In terms of classification performance, it appears evident the discrepancy between the two datasets. The capability of classifiers to recognize the two classes is higher on SNPhotCC and this implies a strong dependency of learning models from the overall accuracy of the simulations. Furthermore, the very similar percentages among the whole feature set and the optimized versions probes the capability of the feature selection method Φ LAB to extract a set of relevant features, able to preserve the level of classification efficiency.

4.7 Superluminous SNe versus SNe I

In the *SNIa Vs SL-I* experiment, the three sub-classes of SNe, Ia, Ia91bg and Iax have been mixed in the same percentage and then classified against Superluminous SNe I. We performed the experiments with the 4 classifiers using all the features and the 78 selected with Φ LAB. The amount of objects per type is shown in Table 18.

The statistical results of the classification are shown in Table 19.

By analyzing the results, it is noticeable the lower performance of Adadelata w.r.t. other classifiers, where Random Forest appeared the best one for all estimators. The

Type	Number of curves	
	Training	Test
SN Ia	9323	2331
SN Iax	9323	2331
SN Ia91bg	9323	2331
SLSN I	27967	6992
Total Ia	27969	6993
Total SL	27967	6992

Table 18 Summary of the objects belonging to the dataset used for the *SNIa Vs SL-I* experiment on PLAsTiCC, randomly partitioned in training (80%) and test (20%) sets.

Features	Random Forest		Nadam		RMSProp		Adadelata		
	All	78	All	78	All	78	All	78	
% Accuracy	-	88	87	81	82	85	82	71	70
% Purity	SL-I	83	80	77	74	81	77	71	70
	SN Ia	93	93	85	89	90	87	71	70
% Completeness	SL-I	94	95	87	92	91	89	71	70
	SN Ia	80	76	74	69	79	74	72	71
% F1 Score	SL-I	88	87	82	82	86	83	71	70
	SN Ia	86	84	79	78	84	80	71	70

Table 19 Summary of the statistical results for the 4 classifiers on the *SNIa Vs SL-I* experiment, with, respectively, all the features and the 78 of the optimized parameter space of PLAsTiCC dataset. For Nadam, RMSProp and Adadelata, the values of 10^{-5} and 0.0005 were assigned to the decay and learning rate hyper-parameters, respectively.

similar results obtained for both parameter spaces confirm the validity of the feature selection.

In terms of error percentages on the SN I class (all Ia sub-types), Table 20 reports the level of contamination for each sub-type in the experiment with all features and using Random Forest.

Class	Total	Correctly classified	Wrongly classified	
SN Ia	2331	2328	3	$\approx 0\%$
SN Iax	2331	1508	823	35%
SN Ia91bg	2331	1779	552	24%

Table 20 Summary of the contamination analysis among all SN Ia sub-types obtained by the Random Forest, with the complete parameter space, on the *SNIa Vs SL-I* experiment.

As shown in Table 20, the most contaminated sub-class is SNIax, which indicates its high difficulty of recognition among other SN types.

4.8 Simultaneous classification of six SNe sub-types

Last classification experiment performed was the most complex, because we tried to classify simultaneously all the six classes of SNe available in the PLAsTiCC dataset. The experiments with the 4 models were performed using all the features and the 78 selected by the optimization procedure. The amount of objects per class is shown in Table 21.

SN Class	Number of curves	
	Training	Test
Ia	27912	6979
Ia91bg	27938	6985
Iax	27981	6996
II	27816	6955
Ibc	27945	6987
SL I	27967	6992

Table 21 Summary of the objects belonging to the dataset used for the *six-class SNe* experiment on PLAsTiCC, randomly partitioned in training (80%) and test (20%) sets.

The statistical results of the six-class classification is reported in Table 22.

Features	Random Forest		Nadam		RMSProp		Adadelta		
	All	78	All	78	All	78	All	78	
% Accuracy	-	66	62	53	55	60	61	48	48
% Purity	SN Ia	79	79	68	71	73	76	62	59
	SN Ia 91bg	82	78	64	70	79	81	52	58
	SN Iax	58	57	46	48	52	51	39	34
	SN II	74	75	58	61	68	66	56	55
	SN Ibc	40	42	32	34	34	35	32	32
	SL SN I	62	59	48	47	56	56	47	50
% Completeness	SN Ia	77	77	56	57	68	67	55	48
	SN Ia 91bg	25	30	27	20	20	17	21	16
	SN Iax	33	37	16	20	26	27	21	15
	SN II	79	79	79	77	77	78	67	67
	SN Ibc	64	57	47	47	54	58	38	47
	SL SN I	91	91	76	88	88	85	85	87
% F1 Score	SN Ia	78	78	62	63	71	71	58	53
	SN Ia 91bg	39	44	38	31	32	28	30	26
	SN Iax	42	45	23	29	35	35	27	21
	SN II	76	77	67	68	72	72	61	60
	SN Ibc	49	48	38	40	42	44	34	38
	SL SN I	73	72	59	62	68	67	61	63

Table 22 Summary of the statistical results for the 4 classifiers on the *six-class SNe* experiment, with, respectively, all the features and the 78 of the optimized parameter space of PLAsTiCC dataset. For Nadam, RMSProp and Adadelta, the values of 10^{-4} and 0.001 were assigned to the decay and learning rate hyper-parameters, respectively.

Also in this case, the Random Forest obtained best results and the similar statistics between the whole and optimized parameter space confirm the good performances of the feature selection method. By analyzing the classification estimators for the single classes, the SNIa91bg showed a high difficulty to be recognized, while Ia91bg and Iax types were often confused for SNIbc. SL type resulted the most complete, although the purity was reduced by the contamination of SNIbc and SNIax (Tab. 23).

		Random Forest Classification						
		Predicted %						
		Ia	Iabg	Iax	II	Ibc	SL	
T r a n s i e n t	Ia	77.3	-	-	22.6	-	0.1	22.7
	Iabg	-	25.3	17.5	-	47.6	9.6	74.7
	Iax	-	2.5	32.6	0.01	45.1	19.7	67.4
	II	21.0	-	-	78.7	0.01	0.3	21.3
	Ibc	0.1	3.0	6.0	0.03	63.9	27.0	36.1
	SL	0.1	0.1	0.3	4.6	4.1	90.8	9.2

Table 23 Percentages of contamination in the *six-class SNe* classification results.

Finally SNIa and SNII types, although reducing their efficiency w.r.t. the dedicated two-class experiment, maintained a sufficient level of classification.

5 Discussion and conclusions

The present work is related to the important problem of classification of astrophysical variable sources, with special emphasis to SNe. Their relevance in terms of cosmological implications is well known, causing a special attention to the problem of recognizing different types of such astronomical explosive events.

To face this challenge, the SNPhotCC dataset and the PLAsTiCC dataset have been chosen to have a statistical sample, albeit of simulations, as wide as possible. Based on the objects in the datasets, a test campaign with increasing complexity has drawn up. To approach the problem we have chosen 4 machine learning methods that require a transformation of light curves into a series of statistical features, potentially suitable to recognize different source types.

In the construction of statistical datasets, the presence of negative fluxes within the observations had to be solved, due to their negative impact on the learning capability of ML models. Working directly with the light curves, their shape is relevant, thus the presence of negative fluxes is not a big problem, because it is always possible to translate the curve along the ordinate axis. In the statistical parameter space instead, since there are features requiring the conversion to magnitudes and since the translation would alter the features values in an unpredictable way, the negative fluxes must be replaced in some way. To solve this problem we tried three approaches, as described in Sec. 4.3. In the first one, the atmospheric and instrumental setup conditions were respected, by grouping the observations taken in the same day;

this solution evidently introduced noise, by altering the phase within groups of light curves. The second solution, which proved to be the best candidate, replaced negative fluxes with a positive number, by maintaining unchanged the sampling, and introducing a lower contribution of noise within data. Finally, the third method removed the observations with negative fluxes, thus highly sub-sampling the light curves. From the classification results obtained adopting the second solution, we were confident that the deformations undergone by the light curves were not able to alter their original nature nor to significantly reduce the performances in both simulation datasets used.

The parameter space analysis was approached with the Φ LAB algorithm to perform a reduction of dimensionality of the classification use cases and to investigate the possibility to identify a common set of features that could be considered suitable to recognize different types of transients. From the comparison between the original and optimized feature spaces, in terms of classification performance, the adopted method resulted extremely reliable to find a reduced set of relevant features, able to preserve the amount of information required to maintain the same level of classification efficiency. Starting from the Φ LAB results, a statistical analysis was performed, which highlighted some interesting aspects related to the physical nature of transients and SNe in particular. The Amplitude feature, representing the semi-difference between the minimum and maximum of the light curve, resulted the most relevant. Since the various classes of SNe have different light peaks, the semi-difference of the amplitude of the curve is typical of each different type of object. Also relevant resulted the standard deviation, MAD, and all features related to the percentiles or characterizing the light curve shape, such as skewness and kurtosis. The relevance of percentiles is related to the different decay time of the light radiation for the various types of SNe. Although a SN is not a periodic event, the feature related to the Lomb-Scargle periodogram has a high importance, because it is able to classify the SNe with a different periods of light decay. On the other hand, all the feature related with thresholds on the number of points around the median (such as the rcb, mr and mbrp), were rejected by our feature analysis method, probably due to their average values too close to their limits.

The most important outcome of the parameter space analysis was the identification of a feature set common to all classification use cases that revealed a coherent behavior in terms of classification performances obtained in all cases, always well close to the efficiency arising from the original parameter spaces.

In terms of pure classification among different types of sources, the high capability to distinguish between Periodic and Non Periodic objects confirmed what expected and posed ML methodology as a good candidate to approach the transient classification problem in Astronomy.

Once removed periodic objects, the high completeness (93%) reached in classifying SNe in the *SNe Vs All* case (Fig. 6), confirmed that ML methods, in particular the Random Forest, could be suitable to distinguish SNe from other transients.

We wanted to verify in the remaining 7%, which was the most contaminating among the different sub-types of SNe; both SNe Ia91bg and SNe Iax were found to have the highest misclassification rate (12% of their test set). Moreover, from this

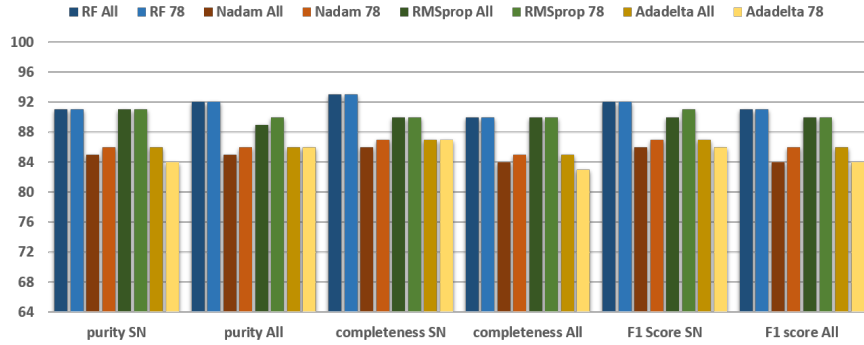


Fig. 6 Histogram of the statistical results (in %) for the *SNe Vs All* classification problem.

analysis it was revealed that SNIa and SNII have an error rate of about 1 per thousand, a remarkable result compared to the other SNe error rates. For completeness, the contamination was also verified for the *All* class, revealing that the AGN type has an error rate of 1 per thousand, while the M-Dwarf and the TDE are the classes with the highest error rates (16%). Further experiments should be carried out to identify the SNe classes with which these two different types of transients are confused and to verify which features play a key role in their classification.

Another interesting case was the classification between Super Luminous (SL) SNe and the mixed Ia types, from which ML appeared able to recognize the SL classification with a completeness, in the best case, of 95% (Fig. 7).

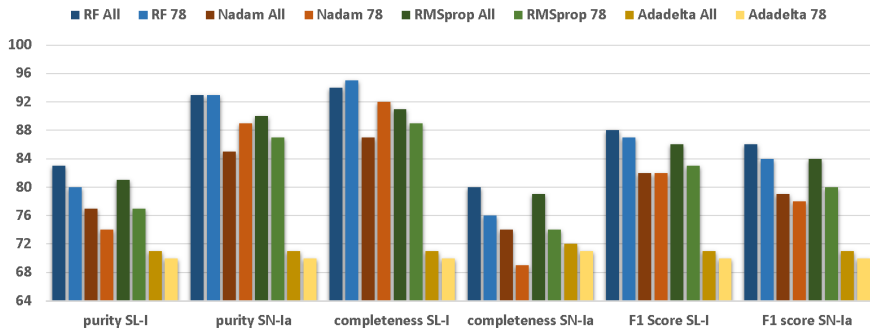


Fig. 7 Histogram of the statistical results (in %) for the *SNIa Vs SL-I* classification problem.

Although further experiments could be in principle performed, from the results obtained in this work, we can suppose to have identified a set of features suitable to help the classification of the SNe Ia, II and SL. However, those able to classify the sub-types Ia91bg and Iax are still unclear. Hopefully, with the availability of real LSST data in the near future, tests with only these two sub-classes could be

conducted, with at most the addition of SNIbc, to evaluate which features could result relevant to recognize such types of SNe.

Acknowledgements The software package of machine learning models used in this work was developed within the DAME project [21]. MB and GR acknowledge the financial contribution from the agreement *ASI/INAF 2018-23-HH.0, Euclid ESA mission - Phase D*, while MB acknowledges also the *INAF PRIN-SKA 2017 program 1.05.01.88.04* and the *MIUR Premiale 2016: MITIC*. Topcat [22] has been used for this work.

References

1. D. Branch, *Nature* **465**(7296), 303 (2010). DOI 10.1038/465303a
2. A. Goobar, B. Leibundgut, *Annual Review of Nuclear and Particle Science* **61**(1), 251 (2011). DOI 10.1146/annurev-nucl-102010-130434
3. S. Huber, S.H. Suyu, U.M. Noebauer, et al., *A&A* **631**, A161 (2019). DOI 10.1051/0004-6361/201935370
4. Z. Ivezić, M.A. Strauss, J.A. Tyson, et al., in *American Astronomical Society Meeting Abstracts #217, American Astronomical Society Meeting Abstracts*, vol. 217 (2011), *American Astronomical Society Meeting Abstracts*, vol. 217, p. 252.01
5. M. Brescia, S. Cavuoti, V. Amaro, et al., in *Data Analytics and Management in Data Intensive Domains*, ed. by L. Kalinichenko, Y. Manolopoulos, O. Malkov, N. Skvortsov, S. Stupnikov, V. Sukhomlin (Springer International Publishing, Cham, 2018), pp. 61–72. DOI 10.1007/978-3-319-96553-6_5
6. M. Brescia, S.G. Djorgovski, E.D. Feigelson, et al., in *Astroinformatics, IAU Symposium*, vol. 325 (2017), *IAU Symposium*, vol. 325
7. M. Brescia, G. Longo, *Nuclear Instruments and Methods in Physics Research A* **720**, 92 (2013). DOI 10.1016/j.nima.2012.12.027
8. L. Breiman, M. Last, J. Rice, in *Statistical Challenges in Astronomy* (Springer New York, New York, NY, 2003), pp. 243–254
9. T. Dozat, in *Proceedings of ICLR Workshop*, vol. 1 (2016), vol. 1, pp. 2013–2016
10. M. Brescia, M. Salvato, S. Cavuoti, et al., *MNRAS* **489**(1), 663 (2019). DOI 10.1093/mnras/stz2159
11. M. Delli Veneri, S. Cavuoti, M. Brescia, et al., *MNRAS* **486**(1), 1377 (2019). DOI 10.1093/mnras/stz856
12. R. Kessler, B. Bassett, P. Belov, et al., *PASP* **122**(898), 1415 (2010). DOI 10.1086/657607
13. K. Ponder, R. Hložek, T. Allam, et al., in *American Astronomical Society Meeting Abstracts, American Astronomical Society Meeting Abstracts*, vol. 52 (2020), *American Astronomical Society Meeting Abstracts*, vol. 52, p. 203.15
14. A.I. Malz, R. Hložek, J. Allam, T., et al., *Astronomical Journal* **158**(5), 171 (2019). DOI 10.3847/1538-3881/ab3a2f
15. The PLAsTiCC team, J. Allam, Tarek, A. Bahmanyar, R. Biswas, et al., arXiv e-prints arXiv:1810.00001 (2018)
16. B. Dilday, R. Kessler, J.A. Frieman, et al., *ApJ* **682**(1), 262 (2008). DOI 10.1086/587733
17. G. Bazin, N. Palanque-Delabrouille, J. Rich, et al., *A&A* **499**(3), 653 (2009). DOI 10.1051/0004-6361/200911847
18. A. D’Isanto, S. Cavuoti, M. Brescia, et al., *MNRAS* **457**(3), 3119 (2016). DOI 10.1093/mnras/stw157. URL <https://doi.org/10.1093/mnras/stw157>
19. L. Breiman, *Machine Learning* **45**(1), 5 (2001). DOI 10.1023/a:1010933404324. URL <https://doi.org/10.1023/a:1010933404324>
20. S.V. Stehman, *Remote Sensing of Environment* **62**(1), 77 (1997). DOI 10.1016/S0034-4257(97)00083-7

21. M. Brescia, S. Cavuoti, G. Longo, et al., *Publications of the Astronomical Society of the Pacific* **126**(942), 783 (2014). DOI 10.1086/677725
22. M.B. Taylor, in *Astronomical Data Analysis Software and Systems XIV*, *Astronomical Society of the Pacific Conference Series*, vol. 347, ed. by P. Shopbell, M. Britton, R. Ebert (2005), *Astronomical Society of the Pacific Conference Series*, vol. 347, p. 29